Enhanced 3-D-Reconstruction Algorithm for C-Arm Systems Suitable for Interventional Procedures

Karl Wiesent*, K. Barth, N. Navab, P. Durlak, T. Brunner, O. Schuetz, and W. Seissler

***Abstract*—Increasingly, three-dimensional (3-D) imaging technologies are used in medical diagnosis, for therapy planning, and during interventional procedures. We describe the possibilities of fast 3-D-reconstruction of high-contrast objects with high spatial resolution from only a small series of two-dimensional (2-D) planar radiographs. The special problems arising from the intended use of an open, mechanically unstable C-arm system are discussed. For the description of the irregular sampling geometry, homogeneous coordinates are used thoroughly. The well-known Feldkamp algorithm is modified to incorporate corresponding projection matrices without any decomposition into intrinsic and extrinsic parameters. Some approximations to speed up the whole reconstruction procedure and the tradeoff between image quality and computation time are also considered. Using standard hardware the reconstruction of a 256^3 cube is now possible within a few minutes, a time that is acceptable during interventions. Examples for cranial vessel imaging from some clinical test installations will be shown as well as promising results for bone imaging with a laboratory C-arm system.**

***Index Terms*—C-arm-based tomography, geometric calibration, homogeneous coordinates, three-dimensional (3-D) image reconstruction.**

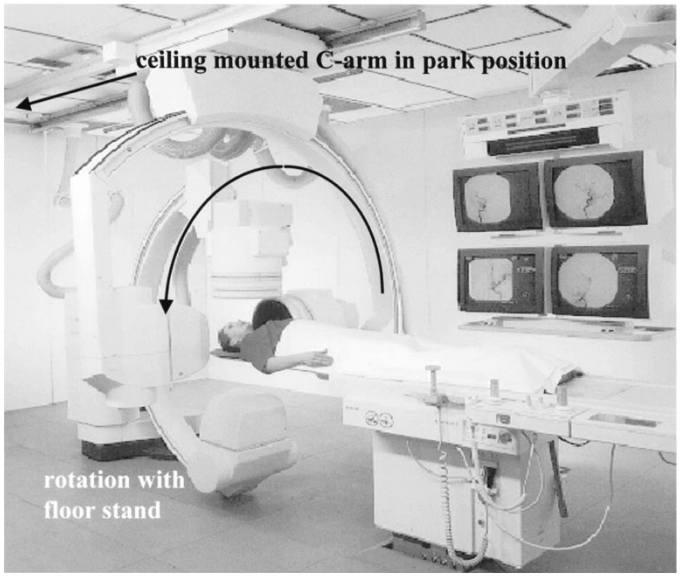

Fig. 1. Siemens NEUROSTAR Plus.

I. Introduction

NEURORADIOLOGY has always been at the forefront in the introduction of new imaging technologies like CT, MR, and PET. For interventional procedures like endovascular techniques, true three-dimensional (3-D)-images of the cranial vessel tree are of great interest for diagnosis and therapy planning. The greatest challenge is the availability of such 3-D information during the interventional procedure. A typical example is the endovascular occlusion of aneurysms using either detachable balloons, liquid occlusion material, or platinum microcoils. We believe that the success of such procedures could benefit from a combination with additional 3-D-imaging capabilities during the intervention. Such an X-ray system must keep the following characteristics: 1) it must have near real-time fluoroscopic capabilities and roadmapping for catheter placement; 2) it must provide accurate anatomical information about the vessel lumen and the location of the embolizing material; and 3) it must allow unobstructed access to the patient during intervention.

As a technical solution, we utilized a standard open C-arm system (Fig. 1), performing a rotation around the object of about 200 degrees, acquiring about 50 radiographic 2-D-projections, and reconstructing a true 3-D-image of the vessel tree within a few minutes. Results from first clinical installations will be shown in Section III. The method may be extended in the future to other medical applications like bone imaging during orthopedic interventions (see Section III for first experimental results).

Research on image intensifier-based tomographic systems, efficient cone-beam reconstruction, and algorithms for true 3-D vessel imaging have a long history, see, e.g., [1]–[4] for earlier work, [5]–[9] for more recent results, and [10]–[12] for first clinical applications. A good description of medical motivation as well as technical challenges can be found in [13] and the references therein. The greatest problems arise from the low number of projections and the irregular sampling patterns caused by the mechanical instability of such systems. The most flexible algorithms to handle irregular geometry and nearly all kinds of pre-information are algebraic methods, see [14], [15] for an overview. A very sophisticated example even capable to handle inconsistent data is described in [16]. For our intended use during intervention, we focus within this paper on sufficiently fast flexible analytical methods for cone-beam geometries with an approximate circular orbit, i.e., modifications

Manuscript received September 1, 1999; revised March 23, 2000. The research on bone imaging was supported in part by Bayerische Forschungs-stiftung. The Associate Editor responsible for coordinating the review of this paper and recommending its publication was M. Defrise. *Asterisk indicates corresponding author*.

*K. Wiesent, K. Barth, P. Durlak, T. Brunner, O. Schuetz, and W. Seissler are with the Medical Engineering Group, Siemens AG, Erlangen/Forchheim, Germany (e-mail: Karl.Wiesent@med.siemens.de).

N. Navab is with Siemens Corporate Research, Inc., Princeton, NJ 08540 USA.

Publisher Item Identifier S 0278-0062(00)05266-6.

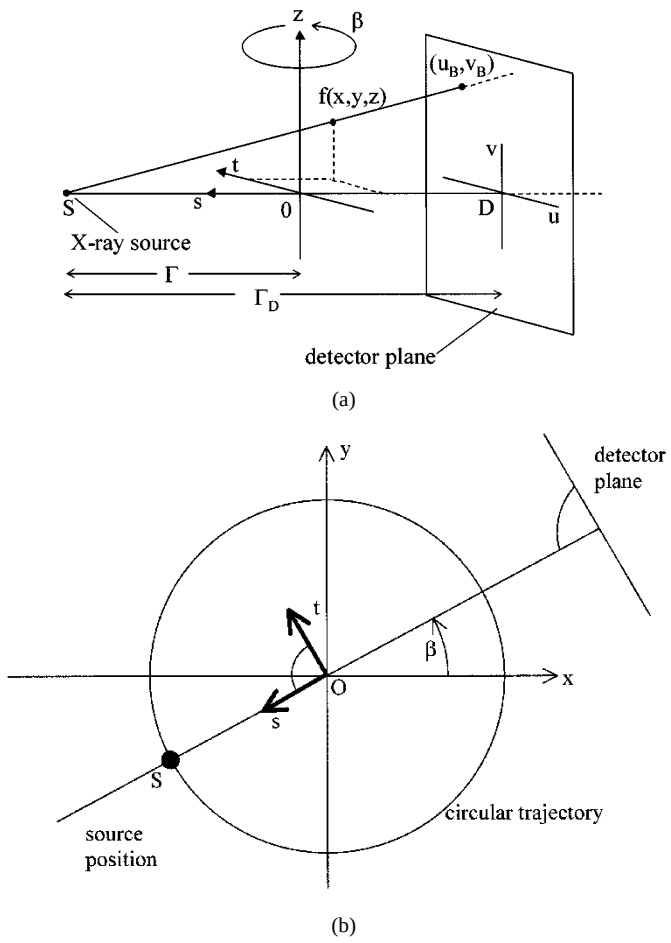

Fig. 2. Original Feldkamp geometry. (a) Perspective view. (b) Midplane.

of the Feldkamp algorithm, see Section II. The algorithms presented there are also useful for similar applications like SPECT [17], microtomography [18], or nondestructive testing [19]. The discussed variants, especially the proposed new backprojection method, may be useful for all of them. Corrections of detector data, like intensity correction and distortion correction of an X-ray image intensifier (XRII), are discussed elsewhere [20], [13]. Also visualization techniques for the 3-D-data sets are not part of this paper.

II. Mathematical Methods

In this section, we will describe some problems and possible mathematical solutions concerning 3-D reconstruction for the considered open systems. Basis will be the well-known algorithm of Feldkamp [2], that was derived for a circular orbit. Therefore, we will refer to this situation as "Feldkamp geometry."

A. Basic Mathematical Model: Ideal Feldkamp Geometry

We start with the following ideal geometry (Fig. 2): The X-ray source S moves on an ideal circle (radius Γ) within the x–y plane around z, the axis of rotation. The (s, t)-system of Fig. 2 denotes the rotated (x, y)-system, β is the angle of rotation. Γ_D is the constant source-to-detector distance. The line from the source position S through the origin O always hits the detector at the origin of its 2-D-coordinate system u–v, and is orthogonal to the detector plane, i.e., it is the so-called optical axis of the X-ray camera. This geometry is the basis of the original Feldkamp algorithm [2]. It can be described by a weighted 1-D convolution

$$\hat{P}_\beta(u, v) = P_\beta(u, v)\,\frac{\Gamma_D}{\sqrt{\Gamma_D^2 + u^2 + v^2}} \tag{1}$$

$$Q_\beta(u, v) = \hat{P}_\beta(u, v) * h(u) \tag{2}$$

followed by a weighted cone-beam backprojection:

$$f(x, y, z) = c \cdot \int_0^{2\pi} \frac{\Gamma^2}{(\Gamma - s)^2}\, Q_\beta(u_B, v_B)\, d\beta \tag{3}$$

with

$$u_B = \Gamma_D t/(\Gamma - s) \quad \text{and} \quad v_B = \Gamma_D z/(\Gamma - s). \tag{4}$$

The input values P_β represent line integrals through the object (logarithms of measured intensities after all pre-corrections). The sequential steps are: cosine weighting (1), 1-D convolution [(2), kernel h like in standard 2-D-CT], and distance weighted backprojection (3). In practical implementations the constant c in (3) is part of the final scaling of the result. For the central x–y plane this algorithm is identical to the well-known exact 2-D-fan-beam algorithm. For other planes it is only an approximate algorithm that however works well for small cone angles. An exact algorithm does not exist, because this sampling geometry violates Tuy's-condition [21]–[23]. For mechanically unstable C-arm systems the deviations from the ideal Feldkamp-geometry cannot be neglected. This will be discussed in the following sections.

B. Classification of Feldkamp Geometries

For further discussion we distinguish the following three types of sampling geometry:

FG1: Ideal Feldkamp geometry
- Source path = complete ideal circle.
- Constant X-ray camera, optical axis perpendicularly hits the origin of the detector.
- Detector rows/columns are orthogonal/parallel to axis of rotation.
- Regular (equidistant) sampling pattern.

FG2: Irregular stable Feldkamp geometry
- Close to ideal geometry, but deviations are not negligible.
- In addition (most cases): Only partial rotation (190–200 degrees).
- But: Constant for repeated experiments (offline calibration possible).

FG3: Unstable Feldkamp geometry
- Irregular and time varying (online PDS necessary)

We use the term PDS (=pose determination system) for any system, that determines the real geometry, either offline as a calibration procedure, or online during data acquisition. In the following, we provide some examples for this classification:

1) Use of a mechanically stable CT-gantry.

Such specialized systems like the Morphometer (assumed perfect XRII-correction), see e.g., [24], are good

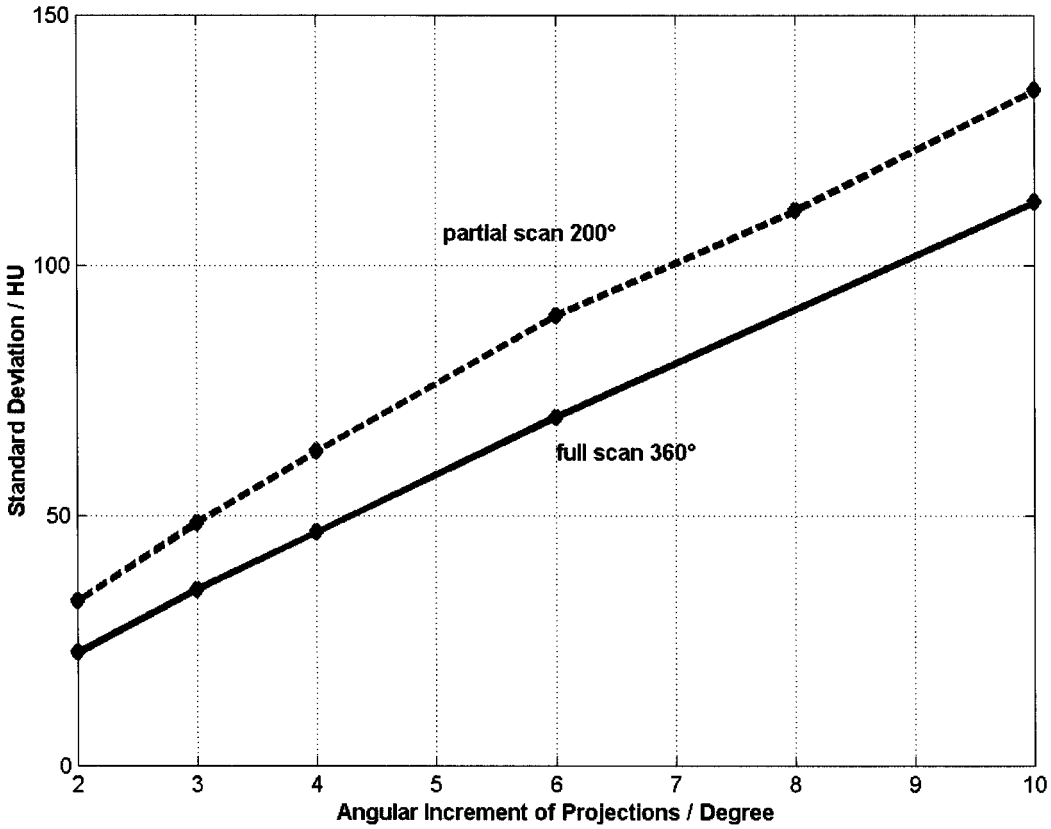

Fig. 3. From simulation study: Artifact level versus angular increment.

for diagnosis, but do not allow unobstructed access to the patient as needed for our intended application during intervention. Class: FG1.

2) Setup with a turn-around table.

   Such systems with fixed X-ray source and detector are widely used in laboratories for basic experiments, see, e.g., [25]. Other examples are microtomography systems for medical applications, e.g., [18], [26], or systems for nondestructive testing [19]. They are class FG1, if the table mount is mechanically perfect, and class FG2 if not, e.g., there is some tilt of the table, which is not negligible.

3) Stable medical C-arm systems.

   It could be shown by experiments, e.g., [27], [13], that some standard C-arm systems work reproducible such that offline calibration is possible. Results from such a system, the Siemens Neurostar Plus, are presented in Section III. These class FG2 machines are the desired devices for high-resolution true 3-D imaging during neurological interventions.

4) Unstable systems.

   In that case, an online PDS must be used. Experiments with such systems of class FG3 are still basic research that can benefit from investigations in robotics and virtual reality. First results from such a laboratory setup are presented in Section III.

The basic imaging system (focal spot + 2-D-detector), the so-called X-ray camera, is usually modeled as an ideal pinhole camera (mathematically: a central perspective mapping, see the Appendix) and can, therefore, be described by a few parameters, the so-called intrinsic parameters. This model and, therefore, the following algorithms can also be used for other systems, like SPECT with focusing collimators or a pinhole aperture. Note, that systems from example 2 have a constant camera, whereas systems of example 3 and 4 in general have a varying camera, because, e.g., the focal length may change due to mechanical instabilities.

C. Low Number of Projections

From sampling theory requirements have been obtained for the ratio M/N (with M = number of projections and N = number of elements within a detector row) to lie between $\pi/2$ and π (but in every case > 1), see, e.g., [28]–[32]. From simulation studies, see Fig. 3, we got the novel result that for M, the number of projections, far below the theoretical recommendations the following linear relationship holds: artifact level $b(M) \sim 1/M$, with $b(M)$ standard deviation of the artifacts measured in HU.

Therefore, accepting an artifact level of, e.g., 100–200 HU, a reconstruction of fine high-contrast objects is possible with only 40–150 projections. With proper windowing for the objects of interest (like bone or vessels filled with contrast agent) these artifacts will not be visible. This is the important difference between normal (low-contrast) CT and high-contrast CT (HCT). The low number of projections generates a natural limit of the low-contrast capabilities of C-arm based tomography. Increasing M, the number of projections, will not increase spatial resolution and morphological information of high-contrast objects, e.g., an opacified vessel tree, but only decrease the ground

artifact level following the above stated linear relationship at the cost of additional patient dose. Low-dose and fast imaging are important features for our intended use during intervention. For diagnosis, when time is not so critical, additional postprocessing methods may be applied, to reduce the basic artifacts. This is still work in progress, for first results see [33].

D. Partial Rotation

From 2-D-fan-beam CT, it is known that a partial rotation over 180° plus fan angle (instead of a full 360° rotation) is sufficient. In that case some data are measured twice. Parker [34] recommended the application of a smooth weighting function for compensation of this effect. Skew rays, typical for Feldkamp geometry, do not really have such redundancies. This problem is discussed, e.g., in [35]. We recommend to compute the Parker weights for the central row of the detector and to supply them without any further modification to all other rows (generalized sinogram weighting).

E. Varying Camera and Sampling Geometry

For the reconstruction task, the actual sampling geometry has to be known precisely. Within the filtering step, the deviation from the ideal case can be neglected—we make a 1-D-convolution row by row as in the ideal Feldkamp algorithm, ignoring a possible small slope of the rows against the x–y-plane—but for backprojection we need the precise geometrical information and have to use it very accurately.

For that we have two general possibilities:

1) Interpolation of the measured data onto ideal measurement geometry. The result can then be interpreted as values from perfect Feldkamp geometry (circular trajectory). Note: For diverging beams this is only approximately true.
2) Modification of the Feldkamp algorithm. Information about the irregular sampling geometry is used within the backprojection step.

In this paper, we concentrate on the second method, because it produces slightly better spatial resolution [36]. The main problem of such mechanically unstable systems is that of accurate pose determination [27], [37], [13]. An imaging system like that of Fig. 2 is normally described by 11 physical parameters, six for the rigid motion of the X-ray camera (extrinsic parameters) and five for the camera itself (intrinsic parameters). Note however, that mathematically these parameters correspond to 10 degrees of freedom, because pixel size of the detector and focal length act as a product and can not be separated. Using homogeneous coordinates (see the Appendix) the 3-D-to-2-D mapping can be described by a single 3×4 matrix $\boldsymbol{P} = [\boldsymbol{AR}, \boldsymbol{At}]$, where $[\boldsymbol{R}, \boldsymbol{t}]$ describes the rigid motion and the upper triangular 3×3 matrix $\boldsymbol{A}$ the camera model in normal position. In our case the intrinsic parameters, e.g., the source detector distance, are not constant. This is an important difference to robotics or virtual reality. One can measure the physical parameters by special procedures [37], [27], [13], [17], or use methods to measure the matrix $\boldsymbol{P}$ directly. One possibility for that is to use a mechanical phantom and to estimate (in a least square sense) $\boldsymbol{P}$ from at least six measured points

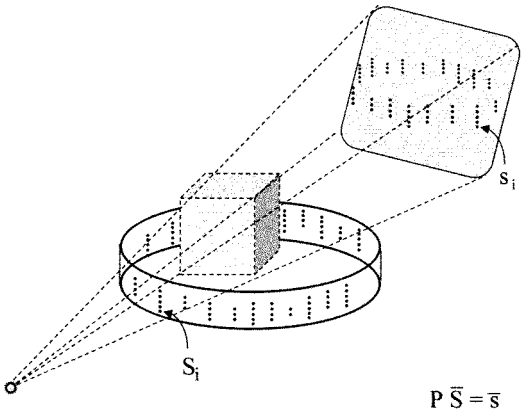

Fig. 4. Projection geometry with marker ring.

[38], [39]. The matrix $\boldsymbol{P}$ can be algebraically decomposed [38], [40] into its intrinsic and extrinsic part (like QR-factorization) and so, if we assume known constant pixel size, all physical parameters of position and of X-ray camera can be determined from $\boldsymbol{P}$. Another method is proposed by Rougee *et al.* [39]. They also use a mechanical calibration phantom to estimate $\boldsymbol{P}$. After that, $\boldsymbol{P}$ is expressed as a nonlinear function of 9 unknown physical parameters and the resulting equation is solved by a conjugate gradient technique.

We use a marker phantom (Fig. 4) and estimate $\boldsymbol{P}$ from about 100–150 points in very high precision. This phantom was originally constructed for online measurements [38], but for stable systems like the Neurostar Plus (Fig. 1) it can also be used for an offline calibration. To summarize: The 3-D-to-2-D mapping of an X-ray projection can be described by a single 3×4 matrix. Knowing the physical parameters, the matrix can easily be computed. If the matrix is given, physical parameters can be calculated from it, if they are needed for sophisticated reconstruction procedures like such of ART type. Our new approach is to use the matrix $\boldsymbol{P}$ without any decomposition and so to avoid errors coming from these additional calculations.

F. Slim Algorithms versus Image Quality

Accepting the dominating artifact level caused by the low number of projections, in HCT some parts of the Feldkamp algorithm may be removed [41]. To discuss this, we first recall all the steps of the proposed reconstruction procedure:

1) Precalculations—like XRII-correction, building logarithms, etc. (not part of this paper). Output of that part are the desired CT-measurement data (line integrals).
2) Preweighting of CT-data—$\Delta\beta_i$ weighting [azimuthal integration, (3)]; cosine weighting [Feldkamp, (1)]; sinogram weighting (Parker).
3) Convolution—$(+)$ optional data extrapolation (if projections are truncated).
4) Backprojection—$(+)$ distance weighting [Feldkamp, (3)].

The highest image quality is naturally achieved by performing all of the above steps and may be further improved by postprocessing methods like [33]. During intervention, a short reconstruction time is essential and morphological information is

much more important than any information about the true density.

Therefore, once having accepted the relatively high ground artifact level caused by the low number of projections, one can remove parts of the above procedure, if the effect of that will be lower than the accepted ground artifacts. Potential candidates for that are all parts except convolution and backprojection, which will be discussed in the next two sections. Spatial resolution of the reconstruction of high contrast objects is only determined by the innermost components of the convolution kernel and exact backprojection. For quantitative imaging without any bias this is not true.

The effect of cancelling out parts of the above procedure is machine and application dependent. For our geometries the cosine weighting can be dropped most easily, because the values are all very close to unity. Azimuthal weighting should be unnecessary, if data acquisition is angle driven and not time driven. Omitting distance weighting during backprojection produces a slight cupping effect, that can be neglected for small reconstruction volumes. Dropping sinogram weighting is much more critical. As already known from 2-D reconstruction, it will produce a butterfly-shaped artifact. For performing this weighting, knowledge of at least one physical parameter, the angle of rotation, is necessary. Clearly, as long as even cancelling some of the weighting steps is considered to be acceptable, small errors in the physical parameters necessary to perform them should not have great significance. Nevertheless, we developed a new accurate method to compute the motion between two projections, and from that the desired parameters, without decomposition of the projection matrices, see Section II-I and [42].

G. Convolution

In most cases, the 2-D detector (XRII or flat panel detector) does not cover the whole object. From such truncated projections severe artifacts may be produced by the usual convolution. To reduce this effect, an extrapolation of the data is a well-known method. We got good results with mirroring the data at both sides. This pseudo-extrapolation does not really enlarge the data set. It can be realized by a simple modification of the convolution procedure similar to [43]. The use of short-range convolution kernels further reduces the propagation of truncation artifacts.

As standard kernel, we used that of Shepp–Logan with full length. It is well known that spatial resolution mainly depends on the central components of the convolution kernel, whereas the outer ones are only necessary for the exact HU-level. In our intended application the physician is interested in anatomical structures and not in quantitative measures. The use of short kernels not only reduces the truncation effect but also saves computation time if filtering is implemented in the spatial domain. The shortest kernels are the unit kernel and the Laplace kernel. They produce the (unfiltered) layergram and the so-called pure λ-reconstruction. Linear combinations of them are known as general λ-reconstruction [44]. For work toward quantitative imaging full-length kernels have to be used.

H. Backprojection in Homogeneous Coordinates

As first shown at the 3-D97-meeting [45], and reported in detail at the 3-D99 meeting [41], backprojection can be written as a sufficiently fast incremental algorithm based on direct use of the projection matrices $\boldsymbol{P}$.

Let $\underline{\boldsymbol{r}} = (\boldsymbol{x}, \boldsymbol{y}, \boldsymbol{z}, \mathbf{1})$ be an arbitrary object point in a given world coordinate system in homogeneous coordinates (for definition, see the Appendix). Then the 3×4 matrix $\boldsymbol{P}$ maps this point to the detector in homogeneous detector coordinates (Fig. 4). After renormalization the units can be interpreted as column-and row-number u and v: This can be written as:

$$\vec{x} \cong P\vec{X} \tag{5}$$

where $\vec{x} = (u, v, 1)$ and $\vec{X} = (x, y, z, 1)$ are the homogeneous coordinates of the 2-D image pixel and the 3-D voxel in the canonical homogeneous coordinate system, respectively. The symbol $\cong$ is used for equality up to scale.

This is identical to what we need in a voxel driven backprojection algorithm. So, the numerically unstable process of decomposing the projection matrix into intrinsic and extrinsic parameters is not necessary. The direct use of the above equation, a multiplication of a 3×4 matrix with a 4-vector $(x_i, y_j, z_k, 1)$ for every voxel would be very inefficient. Because only the final result has to be renormalized (last component to 1) in analytical projective geometry and because of the linearity of the system a sufficiently fast algorithm could be developed.

Let

$$\vec{X} = (x_i, y_j, z_k, 1) = \vec{X}_0 + (i \cdot \Delta x, j \cdot \Delta y, k \cdot \Delta z, 0) \tag{6}$$

describe the position of a voxel. Then we have

$$\vec{x} = P\vec{X} = P\vec{X}_0 + i \cdot \vec{a}_x + j \cdot \vec{a}_y + k \cdot \vec{a}_z. \tag{7}$$

The vectors $\vec{a}_x, \vec{a}_y, \vec{a}_z$ are the first three columns of the projection matrix P multiplied by the corresponding voxel sizes. The result are the homogeneous pixel coordinates (r, s, t) and after renormalization $u = r/t, v = s/t$ we directly have column and row number of the pixel to be backprojected. Thus matrix multiplication has to be performed only once per projection. We summarize the proposed new algorithm by the following pseudocode:

```
For every projection:
• Compute reference point b = (r0, s0, t0)
• Compute auxiliary 3-vectors ax, ay, az
• Loop over voxels:
  do i = 1, nx
   vx = b + i*ax
   do j = 1, ny
    vy = vx + j*ay
    do k = 1, nz
     vz = vy + k*az = (r, s, t)
     u = r/t
     v = s/t
     Backproject imagepoint(u, v)
   end do
  end do
end do
• units of u, v are column and row number,
  the final imagepoint(u, v) then is calcu-
  lated e.g. by bilinear interpolation.
```

Fig. 5. Multiple aneurysms at the internal carotid artery (courtesy Dr. Mawad/Houston). Normal DSA image of the same patient as Fig. 6 (not part of the 3-D-acquisition run of Fig. 6).

Except for the renormalization step in the innermost loop this is a purely incremental algorithm. The combination of describing the geometry, i.e., 3-D-to-2-D mapping, by a single projection matrix $\boldsymbol{P}$ without the use of physical parameters with the above proposed backprojection algorithm is very fast and produces high-quality images. The method is not only used in our C-arm based systems but also in a microtomography system at the University of Erlangen [18].

We summarize the main properties of the new procedure:

- The backprojection is of the voxel driven type (not ray driven).
- The orientation and position of the C-arm motion as well as imaging parameters such as image center and scales along rows and columns are not required.
- The detector may be in arbitrary position, especially not necessarily parallel to the z-axis.
- Even voxel coordinates are never explicitly calculated.

Thus, this algorithm is sufficiently fast and very robust. It is very flexible and not limited to ideal Feldkamp geometry. One example for potential other applications is tomosynthesis [46] with arbitrary sampling pattern.

On the contrary, recently proposed fast backprojection methods [47], [48], based on direct sinogram integration, require special regularity of the considered sampling grids. Fourier methods [23] and methods derived from indirect algorithms [22], needing some interpolation (rebinning) for intermediate functions, also suffer from the low number of projections. The proposed backprojection algorithm needs five FLOPS within the innermost loop for arbitrary geometry, whereas an implementations of the Feldkamp algorithm [23] requires four FLOPS for ideal geometry.

I. Additional Application Specific Calculations in Homogeneous Coordinates

The 3×4 projection matrices can easily be modified. Any change in the world coordinate system can be performed by a matrix multiplication from the right side, changes of the detector coordinate system by a multiplication from the left, but in any case the transformation matrices have to be formulated in homogeneous coordinates. An example for the second one is, that for reconstruction only a part of the original 2-D images is used to further enhance reconstruction speed, e.g., a central rectangle.

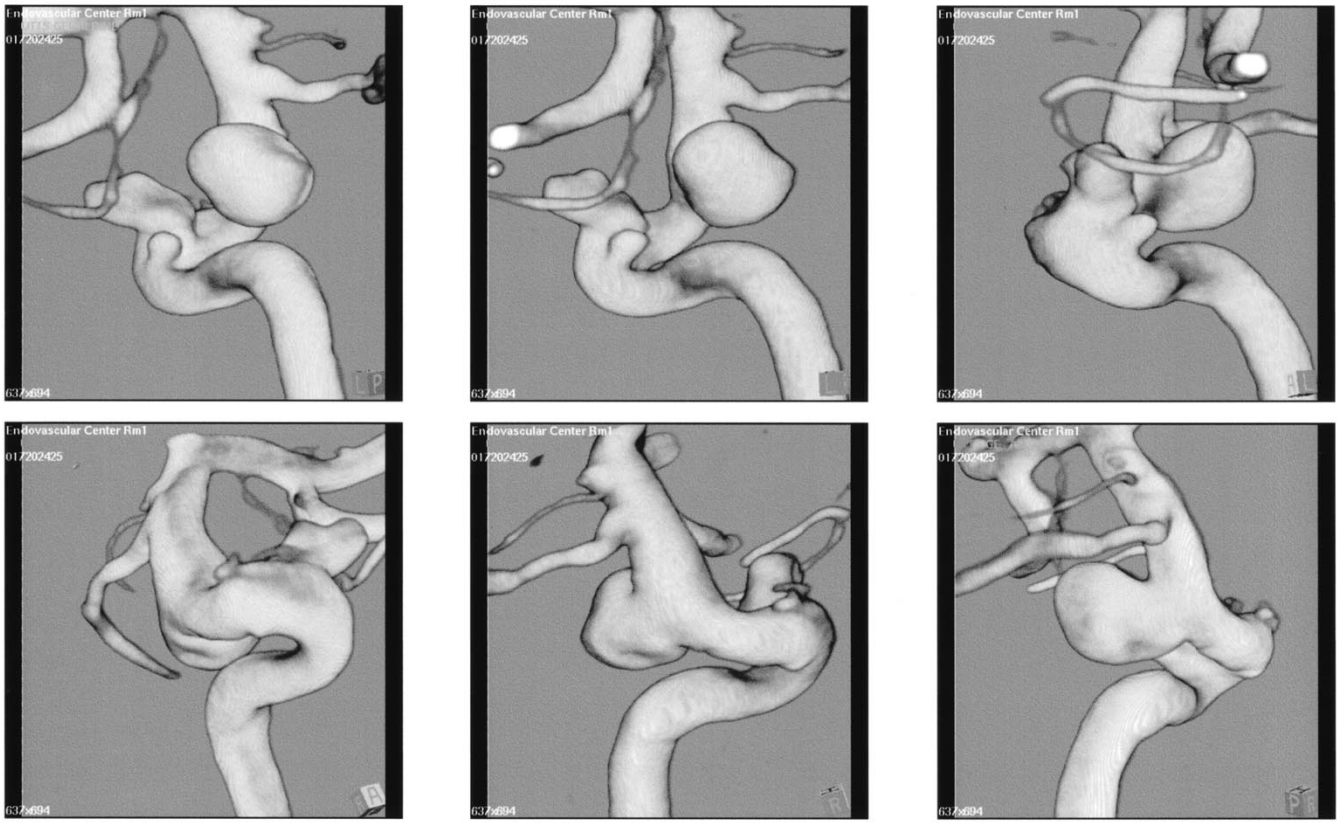

Fig. 6. Multiple aneurysms at the internal carotid artery (courtesy Dr. Mawad/Houston). Volume rendered artificial views from different directions. Same patient as in Fig. 5. Voxel size 0.14 mm, 132 projections.

If dc and dr denote the number of dropped columns and rows from the beginning of the original image, the following matrix will correct the changes in row and column indexing:

$$A = \begin{bmatrix} 1 & 0 & -dc \\ 0 & 1 & -dr \\ 0 & 0 & 1 \end{bmatrix}. \tag{8}$$

Much more important is the problem to establish a natural coordinate frame for the physician. In our standard application the projection matrices are estimated in high precision from the marker ring, see Fig. 4, independent from each other. So the world coordinate system in which $\boldsymbol{P}$ acts, is defined by the location of the PDS during calibration and is not known during later applications, where only the position of the patient relative to the C-arm (iso-center) can be seen. For that we compute the inter-frame rotation between different C-arm positions:

$$P_i \cong P_j \begin{bmatrix} R_{i,j} & t_{i,j} \\ 0 & 1 \end{bmatrix}. \tag{9}$$

From each of these rotations $\boldsymbol{R_{i,j}}$ we can determine an axis of rotation $\boldsymbol{r}$ and an angle of rotation $\boldsymbol{\Delta\beta}$. As described in [42], we developed for these calculations a new accurate method again avoiding matrix decomposition. Now from this information about C-arm motion a new coordinate frame is estimated, which is the best approximation to ideal Feldkamp geometry and to the machine geometry (iso-center). The original projection matrices are all transformed to this new system. After this final step during the calibration procedure, for every projection we provide the following data set:

$\boldsymbol{\Delta\beta}$	angular increment
$\boldsymbol{a_{11}\ a_{12}\ a_{13}\ b_1}$ $\boldsymbol{a_{21}\ a_{22}\ a_{23}\ b_2}$ $\boldsymbol{a_{31}\ a_{32}\ a_{33}\ 1}$	projection matrix
$\boldsymbol{u_1\ u_2\ u_3\ u_4}$	for distance weighting.

The angular information $\boldsymbol{\Delta\beta}$ may be used for sinogram weighting. Scalar multiplication of the vector $\boldsymbol{u}$ with the vector of voxel coordinates (in normalized homogeneous coordinates) gives $\boldsymbol{s}$, with $\boldsymbol{1/s^2}$ being the distance weighting factor (3) of the Feldkamp algorithm. The value of $\boldsymbol{s}$ can also be computed incrementally by simply increasing the dimension of the vectors used in the backprojection algorithm of the last section from 3 to 4. A direct geometric interpretation of the vector $\boldsymbol{u}$ in Fig. 2 would be: $(\boldsymbol{u_1, u_2, u_3}) = \boldsymbol{e}$ = unit vector in direction SO, and $\boldsymbol{u_4} = \boldsymbol{\Gamma} = |\mathrm{SO}|$. Note that source position $\boldsymbol{S}$ can be calculated from the projection matrices $\boldsymbol{P} = \boldsymbol{[AR, At]}$ without decomposition:

$$\boldsymbol{S} = -\boldsymbol{R^t t} = -[\boldsymbol{p_{13}}]^{-1}\boldsymbol{p_4} \tag{10}$$

with 3×3 matrix $[\boldsymbol{p_{13}}] = \boldsymbol{AR}$ from the first three columns of $\boldsymbol{P}$.

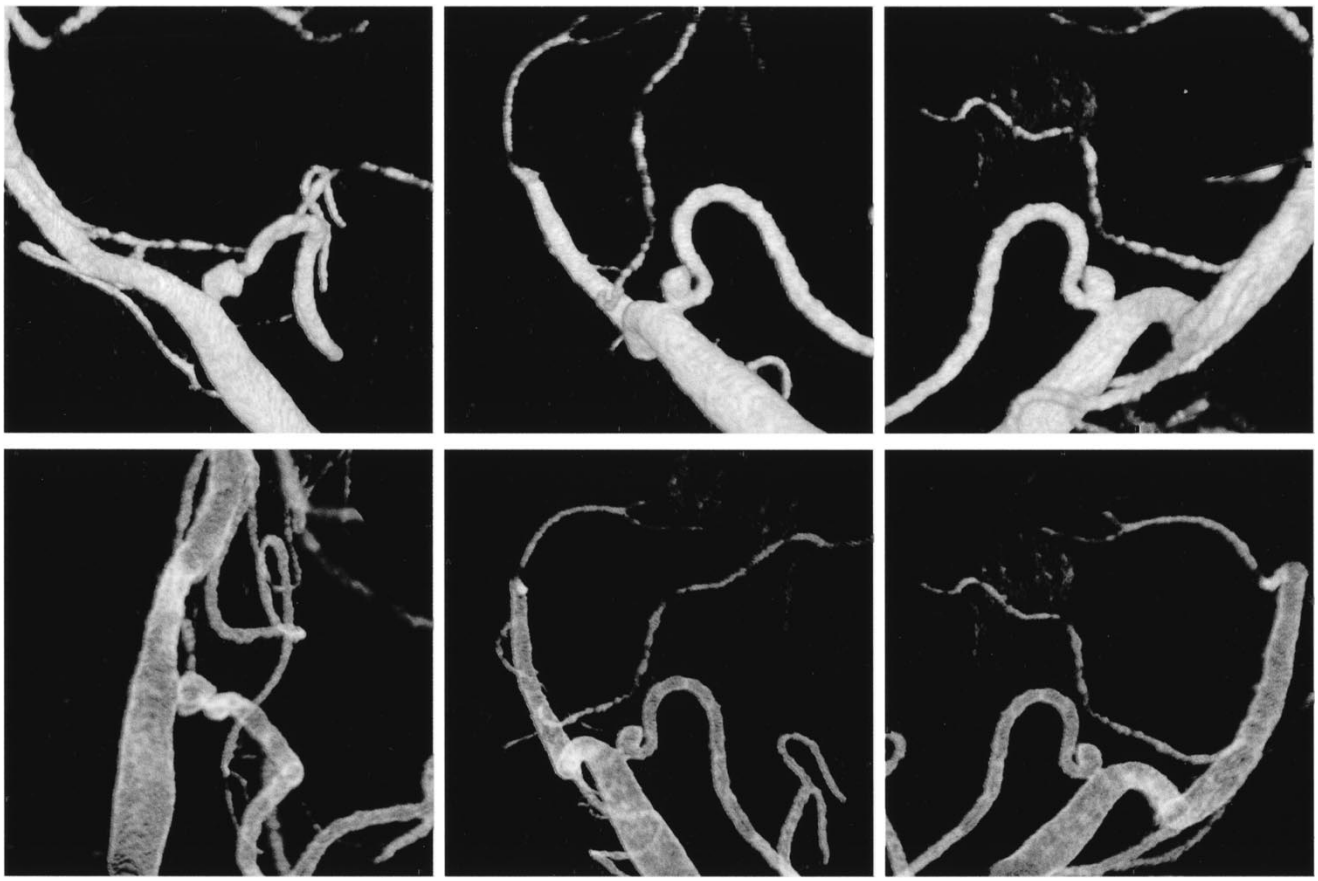

Fig. 7. Aneurysm at the posterior inferior cerebellar artery (courtesy Dr. Böhm-Jurkovic/Linz). Volume rendering: different views and varying opacity. (Upper row) Solid. (Lower row) Translucent. Voxel size 0.24 mm, 50 projections.

III. Results

A. Imaging of Cranial Vessel Trees

The focus of our research, as described in the introduction, is the imaging of cranial vessels. The intended medical application is neuroangiography for diagnosis and interventions (endovascular: dilation, stenting, embolization). Basis is a standard modality, the NEUROSTAR Plus, see Fig. 1. Images from a rotational angiography around the patient's head are transferred to an additional 3-D workstation for preprocessing, 3-D-CT reconstruction, and visualization. Rotation is performed over 200° in 5 s. Selective injection of contrast agent is typically 2.5 ml/s over 5.5 s, in total about 15 ml. An image intensifier with zoom format 22 or 33 cm is used as detector. 2-D-image size is 1024 $\times$ 1024 pixels. The VOI to be reconstructed can be freely selected. Typically, a 256^3cube is reconstructed with an isotropic voxel size of 0.1–0.3 mm.

With a couple of international clinical test installations, the benefit of this new modality has already been proven. Meanwhile, such systems have received a Premarket Notification of the U.S. Food and Drug Administration [510(k)] and are commercially available. Whereas the test systems all worked with 50 projections, the product version also allows to select a higher number. First results from these installations have recently been presented, see, e.g., [49]–[51], [12], or [11] for a journal publication. The main difficulty for the physician is the complex topology of the vessel structures. From a 3-D reconstruction, he or she can interactively generate artificial projections of the VOI from arbitrary directions, even craniocaudal. Figs. 5 and 6 show the same patient with multiple aneurysms at the internal carotid artery. Fig. 5 shows a normal DSA image, Fig. 6 shows a selection of artificial VR-views (VR = volume rendering). In addition, the opacity for the VR can be varied during visualization as shown in Fig. 7, where an aneurysm is shown in "solid" and "translucent" representation. In [11], the authors report about a 3-mo study (40 patients, 49 aneurysms together) comparing normal DSA and rotational angiography with 3-D software. Results (citation from [11]): "In two patients, vessel-loops previously described as aneurysms by DSA could be identified by 3-D angiography. In one patient, an aneurysm was diagnosed that could not be detected by DSA ...." Klucznik/Mawad [12] report: "In all patients, the 3-D imaging added detail and information not possible with routine arteriography." and they conclude: "Three-dimensional rotational angiography will be an indispensable tool for those treating vascular lesions through an endovascular approach." Fig. 8 again demonstrates the ability to clarify a complex topology (multiple aneurysm plus a metal clip from a previous intervention). Surprisingly, there are no severe artifacts from the clip that could destroy the morphological information. Fig. 9 shows an AVM, partially

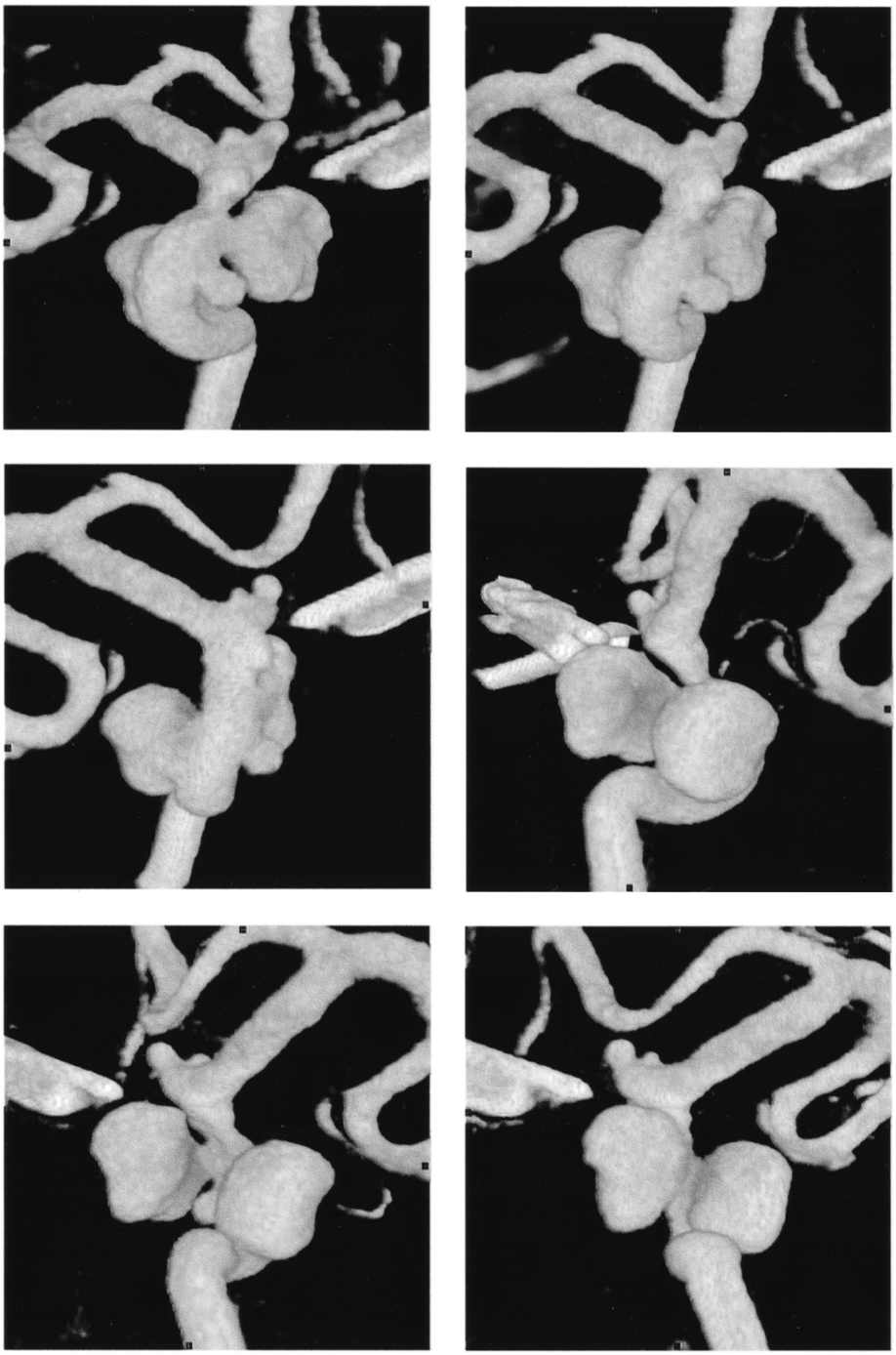

Fig. 8. Multiple aneurysms and metal clip (carotid artery) (courtesy Dr. Berenstein/New York). Volume rendering: different views, voxel size 0.25 mm, 50 projections.

glued, without injection. The catheter visible in the left part of the images has a diameter of 0.25 mm, demonstrating the high spatial resolution available with such systems.

B. Bone Imaging

For investigations on possible further applications like bone imaging, we installed an experimental setup in our laboratory. For that, a movable commercial C-arm system (Siemens SIREMOBIL Compact) has been modified with an additional motor for automatic movement of the C-arm. As detector a prototype of an aSi-panel was mounted. This system is mechanically unstable. For the necessary online PDS we used our mechanical marker ring, but tested also other possibilities, like a new optical method, described in detail in [52], and a method based on a commercially stereoscopic optical camera (Polaris, Northern Digital, Canada). For reconstruction, we used normally 100 2-D images, each with 512×512 pixels. Measurement time was more than 1 min, far beyond the requirements of vessel imaging. Fig. 10 shows a comparison from a reconstruction of a CT bone phantom using the three different systems for pose determination. Fig. 11 shows very promising results from the joint of a

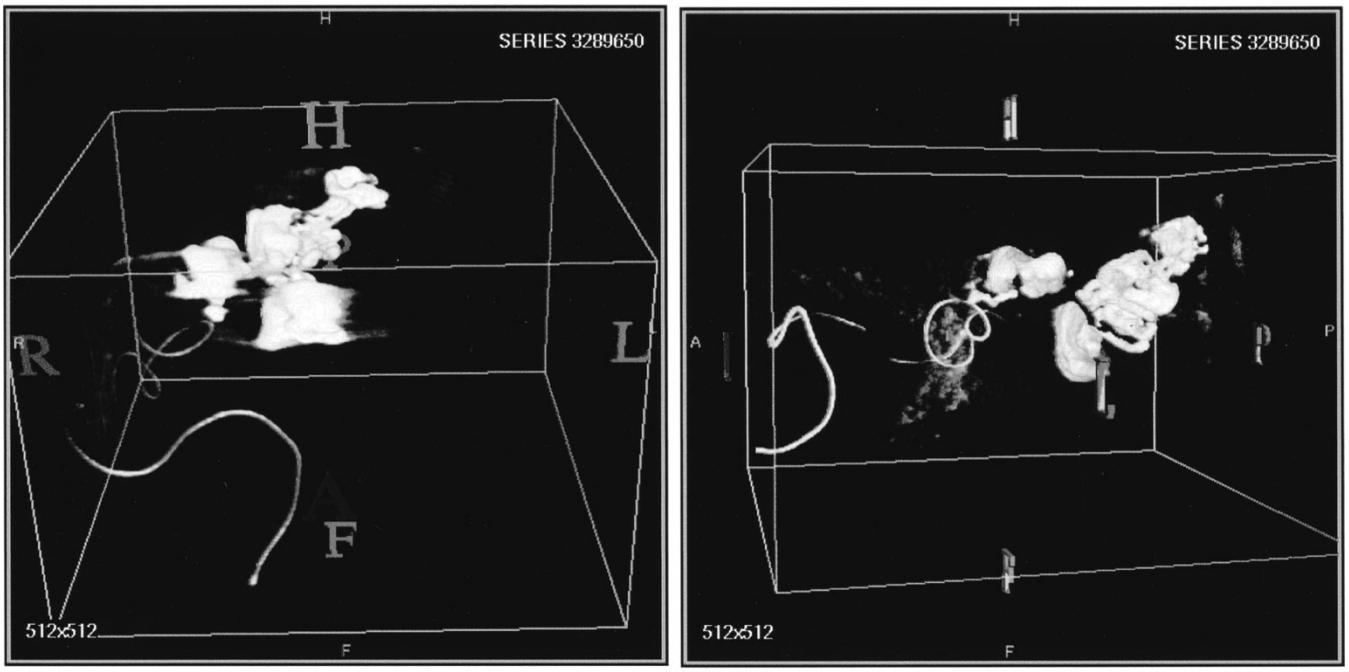

Fig. 9. AVM, partially glued (courtesy Dr. Mawad/Houston). Two volume rendered nearly orthogonal views. No injection, only glue and catheter (0.25 mm) visible. Voxel size 0.21 mm, 132 projections.

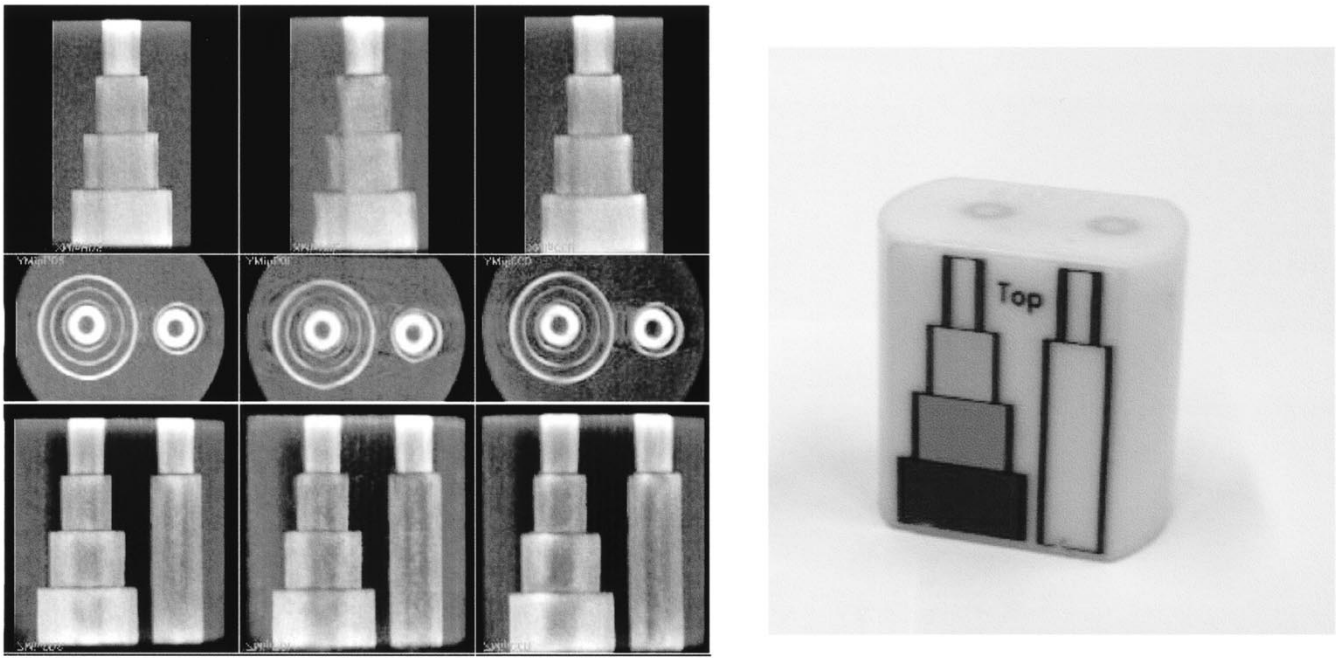

(a) (b)

Fig. 10. Comparison of different pose determination systems. Unstable laboratory setup with 512 × 512 aSi-detector, 3-D reconstruction using different geometrical information. (a) Maximum Intensity Projections of the different results from left to right: mechanical marker ring, Polaris, CCD camera; from top to bottom: x-MIP, y-MIP, z-MIP. (b) Photo of measurement phantom (CT bone calibration phantom).

cow's leg. It seems that for bone imaging, 2-D slices in arbitrary position (MPR technique, known from CT) are much more important than for vessel imaging. These images are first experimental results, from which we believe, that with enhanced online PDS mobile systems with 3-D capability will be realistic in the future.

C. Computation Time

In our laboratory, we used a Siemens PC Celsius 630 with two Pentium III Xeon 550 MHz processors. Reconstructing a 256^3 cube from 100 projections with 512×512 pixels was performed in about 40 s.

Fig. 11. Bone imaging with a joint of a cow's leg. (a) One selected original projection of the object together with the marker ring for pose determination. (b) y-MIP of the reconstructed 3-D VOI. (c) Selected x-slice through the reconstructed volume. (d) Selected y-slice through the reconstructed volume. Voxel size: 0.38 mm, 100 projections.

This time includes a fast convolution in the spatial domain with the proposed data mirroring.

Schaller reported in [18] for the experimental microtomography system of the University of Erlangen a total time of 610 s for reconstructing a 256^3 cube from 180 projections each with 512×512 pixels using a slower single processor Pentium II 233 MHz. He used Intel's DSP library for performing the filtering in the frequency domain.

These two examples show that fast 3-D reconstruction as necessary for use of such systems during intervention is possible with standard hardware.

IV. Conclusion

High-contrast CT (HCT) is possible using X-ray C-arm systems with only 50–100 projections, achieving high accuracy

in only a few minutes. The spatial resolution for such objects (bone or vessels filled with contrast agent) has been shown to be 0.1–0.3 mm. Essential for this is to determine the real geometry of such systems very accurately and to incorporate this information into the reconstruction algorithm. The use of homogeneous coordinates provides a new elegant and fast method, allowing convolution and backprojection to be performed without any explicit use of physical parameters.

Results from laboratory measurements and from several clinical test installations are very promising.

APPENDIX
SHORT REVIEW ON HOMOGENEOUS COORDINATES

For a point $\underline{\boldsymbol{x}}$ in n-D space, we use the following coordinate notations:

$\underline{\boldsymbol{x}} = (x_1, \ldots, x_n)^t$	normal (Euclidean) coordinates
$\underline{\boldsymbol{x}} = (x_1, \ldots, x_n, 1)^t$	normalized homogeneous coordinates
$\underline{\boldsymbol{x}} = (w \cdot x_1, \ldots, w \cdot x_n, w)^t, w \neq 0$	general homogeneous coordinates

For the homogeneous identity, we write $\underline{\boldsymbol{x}} \cong \underline{\boldsymbol{y}}$ iff $\underline{\boldsymbol{x}} = \kappa \underline{\boldsymbol{y}}$ with an arbitrary scalar $\kappa \neq 0$.

In matrix block notation, we now describe some transformations in homogeneous coordinates:

$$H = \begin{bmatrix} A & \underline{0} \\ \underline{0}^t & 1 \end{bmatrix}$$

affine transformation with $\boldsymbol{A}$ an arbitrary $n \times n$ affine transformation matrix. Important examples are: $\boldsymbol{A} = \boldsymbol{R}$ a rotation matrix, and $\boldsymbol{A} = \boldsymbol{S} = \mathbf{diag}(\boldsymbol{s_1}, \ldots, \boldsymbol{s_n})$ a scaling matrix. Let $\boldsymbol{I} = \mathbf{diag}(\mathbf{1}, \ldots, \mathbf{1})$ denote the unit matrix. Then we have

$$T = \begin{bmatrix} I & \underline{t} \\ \underline{0}^t & 1 \end{bmatrix}$$

translation matrix, and

$$M = \begin{bmatrix} R & \underline{t} \\ \underline{0}^t & 1 \end{bmatrix}$$

general rigid motion with rotation matrix $\boldsymbol{R}$ and translation vector $\underline{\boldsymbol{t}}$. Note, that if a pure translation $\underline{\boldsymbol{t}}_{\mathbf{0}}$ is followed by a pure rotation $\boldsymbol{R}$ the translation part of the resulting rigid motion will be $\underline{\boldsymbol{t}} = \boldsymbol{R}\underline{\boldsymbol{t}}_{\mathbf{0}}$.

Any modification of the $(n+1)$th row of the above matrices describes a projective part of a general linear mapping in homogeneous coordinates. We restrict now to $n = 3$ and describe an ideal pinhole camera in its normal position with source at the origin and assumed detector plane perpendicular to the z-axis at $z = d$. We get:

$$P_N = \begin{bmatrix} & I & & \underline{0} \\ 0 & 0 & 1/d & 0 \end{bmatrix} \cong \begin{bmatrix} & d \cdot I & & \underline{0} \\ 0 & 0 & 1 & 0 \end{bmatrix}$$

as the projection matrix, and

$$P_N \begin{pmatrix} x \\ y \\ z \\ 1 \end{pmatrix} = \begin{pmatrix} dx \\ dy \\ dz \\ z \end{pmatrix} \cong \begin{pmatrix} dx/z \\ dy/z \\ d \\ 1 \end{pmatrix}$$

shows how that mapping works.

Cancelling the third row of $\boldsymbol{P_N}$, we get the desired 3-D-to-2-D mapping $\boldsymbol{P} = [\boldsymbol{A_N}, \mathbf{0}]$ with $\boldsymbol{A_N} = \mathbf{diag}(\boldsymbol{d}, \boldsymbol{d}, \mathbf{1})$. This 3×4 matrix $\boldsymbol{P}$ describes the action of our camera in its normal position in world coordinates.

$$B = \begin{pmatrix} \alpha & 0 & a \\ 0 & \beta & b \\ 0 & 0 & 1 \end{pmatrix}$$

describes the transformation to the detector coordinates (scaling to pixel units and shift to the detector origin), and the upper triangular matrix $\boldsymbol{A} = \boldsymbol{B}\boldsymbol{A_N}$ fully describes the camera, and $\boldsymbol{P} = [\boldsymbol{A}, \underline{\mathbf{0}}]$ the mapping in normal position. In general position, we only have to apply a rigid motion $\boldsymbol{M}$, that moves the camera to its normal position, to get the final form of the projection matrices: $\boldsymbol{P} = [\boldsymbol{A}, \underline{\mathbf{0}}]\boldsymbol{M} = [\boldsymbol{AR}, \boldsymbol{A}\underline{\boldsymbol{t}}]$. The entities of $\boldsymbol{A}$ are called intrinsic parameters, that of $\boldsymbol{R}$ and $\underline{\boldsymbol{t}}$ extrinsic parameters of the 3-D-to-2-D mapping of the camera.

REFERENCES

[1] A. C. Kak, C. V. Jakowatz, N. A. Baily, and R. A. Keller, "Computerized tomography using video recorded fluoroscopic images," *IEEE Trans. Biomed. Eng.*, vol. 24, pp. 157–169, 1977.

[2] L. A. Feldkamp, L. C. Davis, and J. W. Kress, "Practical cone-beam algorithm," *J. Opt. Soc. Amer. A*, vol. 6, pp. 612–619, 1984.

[3] R. A. Kruger, D. R. Reinecke, S. W. Smith, and R. Ning, "Reconstruction of blood vessels from x-ray subtraction projections: limited angle tomography," *Med. Phys.*, vol. 14, no. 6, pp. 940–949, Nov./Dec. 1987.

[4] W. J. T. Spyra, A. Faridani, K. T. Smith, and E. L. Ritman, "Computed tomographic imaging of the coronary arterial tree-use of local tomography," *IEEE Trans. Med. Imag.*, vol. 9, pp. 1–4, Mar. 1990.

[5] D. Saint-Felix, Y. Trousset, C. Picard, C. Ponchut, R. Romeas, and A. Rougee, "*In vivo* evaluation of a new system for 3D computerized angiography," *Phys. Med. Biol.*, vol. 39, pp. 583–595, 1994.

[6] R. Ning and R. A. Kruger, "Image intensifier-based computed tomography volume scanner for angiography," *Acad. Radiol.*, vol. 3, pp. 344–350, 1996.

[7] R. Fahrig, A. J. Fox, S. Lownie, and D. W. Holdsworth, "Use of a C-arm system to generate true 3-D computed rotational angiograms: preliminary *in vitro* and *in vivo* results," *Am. J. Neuroradiology*, vol. 18, pp. 1507–1514, 1997.

[8] R. Kempkers, J. Op de Beek, H. Aerts, R. Koppe, E. Klotz, M. Grass, and J. Moret, "3D-rotational angiograhy: first clinical application with use of a standard Philips C-arm system," in *CAR'98*, H. U. Lemke, M. W. Vannier, K. Inamura, and A. Farman, Eds. New York: Elsevier Science, 1998, pp. 182–187.

[9] Y. Trousset, R. Vaillant, L. Launay, J. Obadia, N. Pivet, R. Anxionat, and L. Picard, "A fully automated system for three-dimensional X-ray angiography," in *CARS'99*, H. U. Lemke, M. W. Vannier, K. Anamura, and A. G. Farman, Eds. New York: Elsevier Science, 1999, pp. 39–43.

[10] J. Moret, R. Kemkers, J. Op de Beek, R. Koppe, E. Klotz, and M. Grass, "3D rotational angiography: clinical value in endovascular treatment," *Medica Mundi*, vol. 42, no. 3, pp. 8–14, 1998.

[11] B. Unger, J. Link, J. Trenkler, and H. Böhm-Jurkovic, "Digital 3D rotational angiography in preoperative and preinterventional diagnosis of intracranial aneurysms," *RöFo*, pp. 482–491, Mai 1999. (full paper in German only).

[12] R. P. Klucznik and M. E. Mawad, "Utilization of three-dimensional rotational angiography in the evaluation and endovascular treatment of cerebral aneurysms and arteriovenous malformations," *RSNA 99, Supplement to Radiology*, vol. 213P, p. 276, Nov. 1999.

[13] R. Fahrig, "Computed rotational angiography: Use of a C-arm-mounted XRII for 3D imaging of intracranial vessels during neuro-interventional procedures," dissertation, Univ. Western Ontario, London, Ontario, 1999.

[14] A. Rougée, K. M. Hanson, and D. Saint-Felix, "Comparison of 3D-tomographic algorithms for vascular reconstruction," *SPIE*, vol. 914, Medical Imaging II, pp. 397–405, 1988.

[15] E. Payot, F. J. Preteux, Y. Trousset, and R. Guillemaud, "Generalized support constraint for three-dimensional reconstruction from incomplete Fourier spectra," *J. Electron. Imag.*, vol. 6, no. 4, pp. 426–438, Oct. 1997.

[16] K. M. Andress, "Evidential reconstruction of vessel trees from rotational angiograms," in *IEEE Int. Conf. Image Process.*, Los Alamitos, CA, 1998, pp. 385–389.

[17] Ph. Rizo, P. Grangeat, and R. Guillemaud, "Geometric calibration method for multiple-head cone-beam SPECT system," *IEEE Trans. Nuclear Sci.*, vol. 41, no. 6, pp. 2748–2757, Dec. 1994.

[18] S. Schaller, M. Karolczak, K. Engelke, K. Wiesent, and W. Kalender, "Implementation of a fast cone-beam backprojection algorithm for Micro-CT using homogeneous coordinates," *RSNA 1998, Supplement to Radiology*, vol. 209P, pp. 433–434, Nov. 1998.

[19] K. J. Kyriakopoulos, P. Yiannakos, V. Kallipolites, and K. Domales, "A geometric calibration methodology for single-head cone-beam X-ray systems," *J. Intell. Robot. Syst.*, vol. 24, pp. 151–174, 1999.

[20] R. Fahrig, M. Moreau, and D. W. Holdsworth, "Three-dimensional computed tomographic reconstruction using a C-arm mounted XRII: correction of image intensifier distortion," *Med. Phys.*, vol. 24, no. 7, pp. 1097–1106, July 1997.

[21] H. Tuy, "An inversion formula for cone-beam reconstruction," *SIAM J. Appl. Math.*, vol. 43, pp. 546–552, 1983.

[22] P. Grangeat, P. Sire, R. Guillemaud, and V. La, "Indirect cone-beam three-dimensional image reconstruction," in *Contemporary Perspectives in Three-Dimensional Biomedical Imaging*, C. Roux and J. L. Coatrieux, Eds. Amsterdam: IOS, 1997.

[23] C. Jacobson, "Fourier methods in 3D-reconstruction from cone-beam data," Linköping Studies in Science and Technology Dissertations no. 427, 1996.

[24] Y. Trousset, C. Picard, C. Ponchut, R. Romeas, R. Campagnolo, S. Croci, J. M. Scarabin, and M. Amiel, "3D X-ray angiography: from numerical simulations to clinical routine (invited paper)," in *Proc. 1995 Int. Mtg. Fully Three-Dimensional Image Reconstruct. Radiol. Nuclear Med.*, Aix-les-Bains, July 4–6, 1995, pp. 3–9.

[25] R. Ning, "The construction and evaluation of a prototype system for an image intensifier-based system," dissertation, Univ. Utah, 1989.

[26] R. H. Johnson, J. Hsieh, R. C. Molthen, and C. A. Dawson, "Efficacy of beam-hardening correction for vascular morphometry using 3D conebeam micro-CT," in *Proc. 1999 Int. Mtg. Fully Three-Dimensional Image Reconstruct. Radiol. Nuclear Med.*, Egmond aan Zee, June 23–26, 1999, pp. 208–211.

[27] R. Fahrig, A. J. Fox, and D. Holdsworth, "Characterization of a C-arm mounted XRII for 3D image reconstruction during interventional neuroradiology," *Proc. SPIE*, vol. 2708, pp. 351–360, 1996.

[28] P. M. Joseph and R. A. Schulz, "View sampling requirements in fan beam tomography," *Med. Phys.*, vol. 7, pp. 692–702, Nov./Dec. 1980.

[29] H. H. Barrett and W. Swindell, *Radiological Imaging*. New York: Academic Press, 1981.

[30] G. Schwierz, W. Haerer, and K. Wiesent, "Sampling and discretization problems in X-ray CT," in *Mathematical Aspects of Computerized Tomography, Proc. Oberwolfach 1980*. New York: Springer, 1981, vol. 8, Lecture Notes in Medical Informatics, pp. 292–309.

[31] F. Natterer, *The Mathematics of Computerized Tomography*. Stuttgart: Teubner, 1986.

[32] ——, "Numerical methods in tomography," *Acta Numerica*, 1999.

[33] R. R. Galigekere, K. Wiesent, and D. W. Holdsworth, "Techniques to alleviate the effects of view aliasing artifacts in computed tomography," *Med. Phys.*, vol. 26, no. 6, pp. 896–904, 1999.

[34] D. L. Parker, "Optimal short scan convolution for fanbeam CT," *Med. Phys.*, vol. 9, pp. 254–257, 1982.

[35] G. L. Zeng and G. T. Gullberg, "Short-scan cone beam algorithm for circular and noncircular detector orbits," *SPIE*, vol. 1233, Medical Imaging IV: Image Process., pp. 453–463, 1990.

[36] R. Fahrig and D. W. Holdsworth, "Three-dimensional computed tomographic reconstruction using a C-arm mounted XRII: image-based correction of gantry motion nonidealities," *Med. Phys.*, vol. 27, no. 1, pp. 30–38, 2000.

[37] R. Koppe, E. Klotz, J. Op de Beek, and H. Aerts, "3D vessel reconstruction based on rotational angiography," in *Computer Assisted Radiology, Proc. Int. Symp., CAR'95 Berlin*, H. U. Lemke, K. Inamura, C. C. Jaffe, and M. V. Vannier, Eds. New York: Springer Verlag, 1995, pp. 101–107.

[38] N. Navab, A. Bani-Hashemi, M. Mitschke, A. J. Fox, D. W. Holdsworth, R. Fahrig, and R. Graumann, "Dynamic geometrical calibration for 3-D cerebral angiography," *SPIE*, vol. 2708, pp. 361–370, 1996.

[39] A. Rougée, C. Picard, Y. Trousset, and C. Ponchut, "Geometrical calibration for 3D X-ray imaging," *SPIE*, vol. 1897, Image Capture, Formatting, and Display, pp. 161–169, 1993.

[40] O. D. Faugeras, *Three-Dimensional Computer Vision: A Geometric Viewpoint*. Cambridge, MA: MIT Press, 1993.

[41] K. Wiesent, K. Barth, N. Navab, T. Brunner, and W. Seissler, "Enhanced 3D-reconstruction algorithms for C-arm based interventional procedures," in *Proc. 1999 Int. Mtg. Fully Three-Dimensional Image Reconstruct. Radiol. Nuclear Med.*, Egmond aan Zee, June 23–26, 1999, pp. 167–170.

[42] N. Navab, A. Bani-Hashemi, M. S. Nadar, K. Wiesent, P. Durlak, T. Brunner, K. Barth, and R. Graumann, "3D reconstruction from projection matrices in a C-arm based 3D-angiography system," in *MICCAI'98, Proceedings*, W. M. Wells, A. Colchester, and S. Delp, Eds. New York: Springer, 1998, pp. 119–129.

[43] B. M. Ohnesorge, T. Flohr, K. T. Bae, and J. P. Heiken, "An efficient correction for artifacts in CT images caused by objects extending beyond the scanfield of view," *RSNA 1998, Supplement to Radiology*, vol. 209P, p. 435, Nov. 1998.

[44] A. Faridani, E. R. Ritman, and K. T. Smith, "Local tomography," *SIAM J. Appl. Math.*, vol. 52, no. 2, pp. 459–484, April 1992.

[45] K. Wiesent, R. Graumann, R. Fahrig, D. W. Holdsworth, A. J. Fox, N. Navab, and A. Bani-Hashemi, "3D-reconstruction during interventional neurological procedures," in *Proc. 1997 Int. Mtg. Fully Three-Dimensional Image Reconstruct. Radiol. Nuclear Med.*, Nemacolin Woodlands, 1997.

[46] G. Lauritsch and W. Härer, "A theoretical framework for filtered backprojection in tomosynthesis," *SPIE*, vol. 3338, Conf. Image Process., pp. 1127–1137, Feb. 1998.

[47] M. Ingerhed, "Fast backprojection for computed tomography," dissertation, Univ Linköping, 1999.

[48] H. Turbell and P. Danielsson, "Fast Feldkamp reconstruction," in *Proc. 1999 Int. Mtg. Fully Three-Dimensional Image Reconstruct. Radiol. Nuclear Med.*, Egmond aan Zee, June 23–26, 1999, pp. 311–314.

[49] T. Brunner, P. Durlak, K. Barth, K. Wiesent, R. Graumann, H. Barfuß, A. Bani-Hashemi, N. Navab, and M. Nadar, "3D reconstruction of cerebral vessels based on a rotational angiography with a C-arm," *ECR'99, Supplement 1 to Euro. Radiol.*, vol. 9, p. 167, 1999.

[50] U. Missler and T. E. Mayer, "Clinical evaluation of 3D reconstructed rotational DSA for treatment planning of intracranial aneurysms," *RSNA 98, Suppl. Radiol.*, vol. 209P, p. 155, Nov. 1998.

[51] M. Skalej, U. Ernemann, and K. Barth, "3D-reconstructions of intracranial vessel trees based on a rotational angiography imaging system," *RSNA 98, Suppl. Radiol.*, vol. 209P, p. 156, Nov. 1998.

[52] N. Navab, M. Mitschke, and O. Schütz, "Camera-augmented mobile C-arm (CAMC) application: 3D reconstruction using a low cost mobile C-arm," in *Medical Image Computing and Computer-Assisted Intervention—MICCAI '99*, C. Taylor and A. Colchester, Eds. New York: Springer, 1999, pp. 688–697.